Engineering model for coupling wicks and electroosmotic pumps with proton exchange membrane fuel cells for active water management

Shawn Litster [1], Cullen R. Buie [2], Juan G. Santiago *

Department of Mechanical Engineering, Stanford University, Stanford, CA 94305, USA

ABSTRACT

We present theoretical and experimental studies of an active water management system for proton exchange membrane (PEM) fuel cells that uses integrated wicks and electroosmotic (EO) pumps. The wicks and EO pumps act in concert to remove problematic excess liquid water from the fuel cell. In a previous paper, we showed that this system increases maximum power density by as much as 60% when operating with low air stoichiometric ratios and a parallel channel flow field. The theoretical model we develop here accounts for several key factors specific to optimizing system performance, including the wick's hydraulic resistance, the variation of water pH, and the EO pump's electrochemical reactions. We use this model to illustrate the favorable scaling of EO pumps with fuel cells for water management. In the experimental portion of this study, we prevent flooding by applying a constant voltage to the EO pump. We experimentally analyze the relationships between applied voltage, pump performance, and fuel cell performance. Further, we identify the minimum applied pump voltage necessary to prevent flooding. This study has wide applicability as it also identifies the relationship between active water removal rate and flooding prevention.

1. Introduction

Achieving proper water management in PEM fuel cells with perfluorosulfonic acid (PFSA) membranes (e.g., Nafion) without compromising system efficiency remains a significant technical impediment to commercialization [1]. Design and operation of fuel cells with these membranes requires careful consideration of the internal humidity. For example, a Nafion membrane in an 80% relative humidity environment has close to half the conductivity of the same membrane in a 100% relative humidity environment [2]. However, with high humidity levels, the oxygen reduction reaction at the cathode produces liquid water that inhibits reactant diffusion through the gas diffusion layers (GDLs) and catalyst layers and causes flow maldistribution in flow fields having multiple channels. A common strategy for minimizing liquid water flooding is to use a low number of serpentine channels in lieu of many parallel channels [3]. Employing serpentine channels increases local gas velocities and improves advective removal of water droplets. Sim-

ilarly, high air flow rates improve water removal. However, both strategies increase the parasitic load associated with air pumping power, which is nominally the largest parasitic load on automotive fuel cell systems [4]. In addition, the use of high air stoichiometric ratio complicates system design because of the greater amount of water required to humidify the air.

There have been several unique passive [5,6] and active [7] approaches to water management, reviewed in Ref. [8]. Buie et al. [9] first demonstrated the removal of water from a PEM fuel cell using EO pumps. In that work, EO pumps were integrated within the channel walls of a single channel 1.2 cm² fuel cell. As Fig. 1a depicts, EO pumps generate flow when an electric field is applied across a porous glass substrate. EO flow is due to the coupling between an externally applied electric field and the charges of an electric double layer (EDL) which forms at the interface between liquids and solids. The applied electric field imposes a Columbic force on the diffuse layer of positive ions of the EDL and the motion of these charges drives a bulk flow through viscous interactions. In Litster et al. [8], we presented a new approach to water management using integrated wicking structures and an external EO pump to actively manage liquid water in PEM fuel cells.

Fig. 1b presents a cut-away schematic of the 25 cm² fuel cell with an integrated wick and external EO pump and illustrates the water removal pathway. Water produced within the membrane electrode assembly (MEA) is absorbed into the porous carbon wick and EO pump by capillary action. The porous carbon wick also serves as the air flow field "plate" and cathode current collector. The 0.5 mm thick

* Corresponding author at: Building 530, Room 225, 440 Escondido Mall, Stanford, CA 94305, USA. Tel.: +1 650 723 5689; fax: +1 650 723 7657.
E-mail addresses: litster@andrew.cmu.edu (S. Litster), crb@mit.edu (C.R. Buie), juan.santiago@stanford.edu (J.G. Santiago).
[1] Present address: Department of Mechanical Engineering, Carnegie Mellon University, Pittsburgh, PA 15213, USA.
[2] Present address: Department of Mechanical Engineering, Massachusetts Institute of Technology, Cambridge, MA 02139, USA.
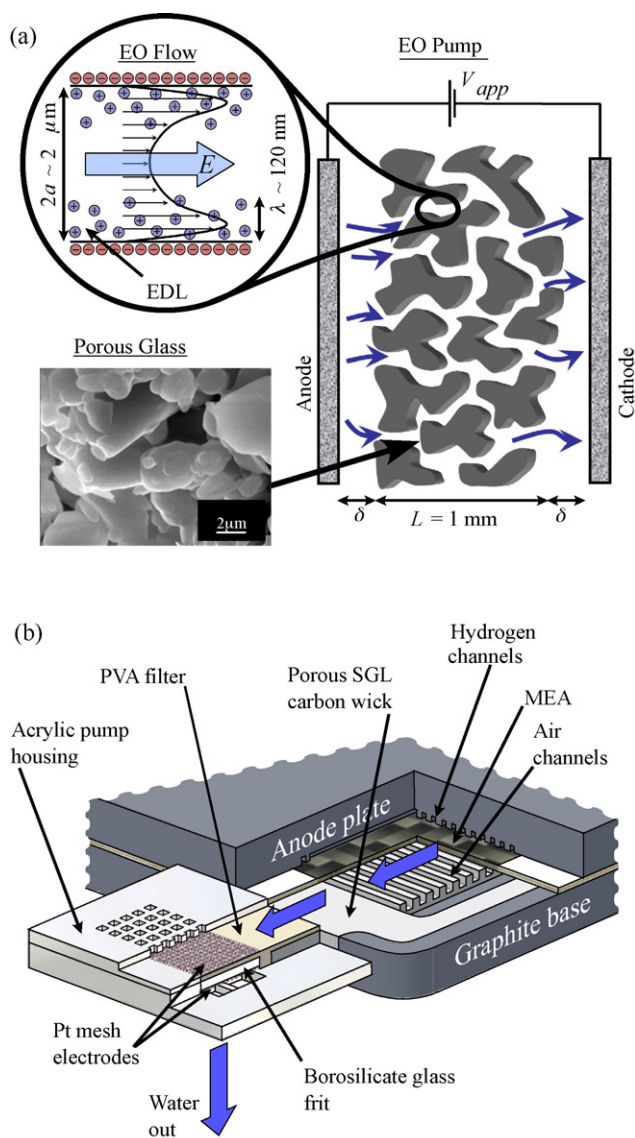
Fig. 1. (a) Schematic of EO flow in a porous glass EO pump. We form the EO pump by placing electrodes on either side of a porous glass substrate. The main schematic depicts flow through the porous glass substrate. A scanning electron micrograph (SEM) of the porous glass is shown in the bottom left. When saturated with water, the walls of the porous glass generate a negative charge and an EDL forms (schematic in upper left). The external electric field, *E*, imposes a Columbic force on the EDL's diffuse layer of positive charges and generates bulk flow by viscous interaction. (b) Cut-away schematic of the fuel cell assembly with an integrated porous carbon wick and an external 2 cm^2 EO pump. Water produced in the fuel cell's MEA wicks into the porous carbon until the wick and EO pump substrate are saturated. With a voltage applied across the mesh electrodes, the pump generates a local suction pressure in the wick that actively draws excess water from the cathode channels and GDL.

layer of porous carbon connecting the channel ribs allows liquid water to travel perpendicular to the channels rather than along the channels, which reduces the water's path length to the pump. The EO pump is coupled to the porous carbon via a polyvinyl alcohol (PVA) wick, which separates the electric currents of the fuel cell and EO pump. Once water saturates the porous borosilicate glass, the electric circuit between the platinum mesh electrodes of the EO pump is closed and the pump generates a suction pressure that pulls excess liquid water out of the fuel cell.

In Ref. [8], we demonstrated the ability of the wick and EO pump system to prevent flooding in a PEM fuel cell with a large number of parallel channels over a wide range of air stoichiometric ratios and current densities. The parasitic losses due to EO pumping were

typically less than 0.5% of the fuel cell power. We gauged fuel cell performance enhancement with EO pumping by comparing this fuel cell's polarization curves with those of the fuel cell with the identical channel design and either no EO pumping or a non-porous flow field. At a low, efficient air stoichiometric ratio of 1.3, this system yielded a 60% increase in maximum power density. Strickland et al. [10] investigated the effect of active water management with EO pumps on the spatial distribution of current using a segmented anode plate.

In this paper, we provide a theoretical model to aid the design of these coupled devices and evaluate the scaling between EO pumps, wicks, and fuel cells. We present experimental results to support the theoretical model and investigate relationships between fuel cell performance and water removal rates. In this work, the EO pump operates with a constant applied voltage.

2. Theory

EO pumps are well suited to actively removing water from PEM fuel cells because of their small volume, low power requirement, and lack of moving parts. For a given application, the efficacy of pumping with electroosmosis depends on the four disparate length scales depicted in Fig. 1a. First, EO flow requires the presence of the nano-scale EDL at the interface between the liquid and the glass substrate. The EDLs of interest here have characteristic length scales of the order of 100 nm (consistent with water exposed to atmospheric air). Second, to generate adequate pressures with electroosmosis, the diameter of the pores must be sufficiently small to restrict the reverse flow generated by a pressure load (here our mean pore diameter is 2.0 μm). The third important length scale is the thickness of the pump substrate (here 1 mm). The average velocity in the pores depends on the local electric field and the local pressure gradient, which are both inversely proportional to pump thickness. The fourth length scale relates to the cross-sectional area of the EO pump because the flow rate is proportional to pump area (here we use a 2 cm by 1 cm pump).

Modeling a coupled fuel cell and EO pump system requires careful consideration of each of these physicochemical systems. Our present analysis is a significant extension of our previous work [9,11,12] in that we consider four additional factors: (1) the electrochemistry of pump electrodes; (2) the details of multi-dimensional water transport through the wick; (3) the effects of pressure-driven advective current in the pump (in addition to EO-driven advective and electromigration currents), and (4) the effects of EO pumping on pH and pump surface zeta potentials. In the next section, we summarize the key relation for pressure–load-specific flow rate from our previous work [9,11]. In the subsequent sections, we present the extensions listed above.

2.1. EO pumps: flow rate as a function of pressure load

To model EO pumps, we leverage the fact that the velocities of EO flow and the reverse, pressure-driven flow can be superposed linearly [13]. Yao and Santiago [11] modeled the flow rate, Q_{eo}, of a porous glass EO pump as flow through an array of cylindrical capillaries by accounting for the area, A_{eo}, porosity, ψ, and tortuosity, τ, of the porous pumping substrate. They provided the following relation for the flow rate, Q_{eo}:

$$Q_{eo} = A_{eo} \frac{\psi}{\tau} \left[-\frac{a^2}{8\mu_l} \frac{\Delta p}{L} - \frac{\varepsilon \zeta f}{\mu_l} \frac{V_{eff}}{L} \right] \qquad (1)$$

where μ_l is the liquid viscosity, Δp is the pressure drop across the pump, L is the thickness of the substrate, ε is the liquid permittivity, and ζ is the zeta potential. The non-dimensional factor f accounts for the effect of the EDL's finite thickness on the velocity profile

in the pores [11]. This finite potential distribution can be solved analytically with the Debye–Hückel approximation [14] or with the more accurate numerical solution used here [11]. The details of the numerical approach are described by Yao and Santiago [11] and Kim et al. [15].

2.2. Effects of pump electrode spacing and activation overpotential

The effective voltage drop across the pumping substrate, V_{eff}, in Eq. (1) is the applied voltage, V_{app}, subtracted by both the decomposition voltage, V_{dec}, and the Ohmic voltage loss associated with conduction through the region separating the electrodes and the pump. The decomposition voltage is a complex function of the reaction rate and the electrolyte and electrode properties (including material, geometry, and surface conditions). It consists of the reaction's reversible potential, V_{rev}, and the anode and cathode activation overpotentials, η_{an} and η_{ca}:

$$V_{dec} = V_{rev} + \eta_{an} + \eta_{ca} \tag{2}$$

In most models of EO pumping [11] the decomposition voltage is treated as an empirical constant, which is acceptable for predicting high voltage operation. However, here we are particularly interested in low voltage operation and account for the current dependent electrode overpotentials with the Tafel equation [16]:

$$V_{dec} = V_{rev} + b_{eo} \, \ln\left(\frac{I_{eo}}{r_A A_{eo} j_{o,eo}}\right) \tag{3}$$

where I_{eo} is the EO pump current and b_{eo} and $j_{o,eo}$ are the Tafel slope and exchange current density for the EO pump, respectively. The parameter r_A is the ratio of actual electrode surface area to planar electrode area. For electrolysis in acidic conditions, the oxygen evolution reaction is significantly slower than the hydrogen evolution reaction and dominates the activation overpotential [17]. Thus, we model the total activation overpotential with values of the Tafel slope and exchange current density for the oxygen evolution reaction in acidic conditions on a Pt electrode [17,18]. In this study, the estimated decomposition voltage ranges between 2 and 3 V, depending on the magnitude of the current.

We must also account for Ohmic voltage drop in the spaces between the electrodes and porous glass when calculating the effective voltage. In the experiments, the cathode mesh electrode was directly against the frit, while the 0.6 mm thick (compressed) PVA wick separated the anode from the frit. The porous PVA reduces the effective conductivity in the spacing according to its compressed porosity, $\psi_{PVA,c}$, and tortuosity, τ_{PVA}. To calculate the effective voltage, we take the difference between the applied voltage and the decomposition voltage and multiply it by the ratio of substrate resistance to total resistance between the electrodes:

$$V_{eff} = (V_{app} - V_{dec})\frac{L}{\tau_{PVA}\gamma\delta/\psi_{PVA,c} + L} \tag{4}$$

The parameter γ accounts for the effects of porosity, tortuosity, and finite EDLs on the effective conductivity in the frit. The following expression predicts γ:

$$\gamma = \frac{\psi f}{\tau g} \tag{5}$$

where g is the non-dimensional effect of the finite EDL on flow rate per current ratio as defined by Yao and Santiago [11].

2.3. Hydraulic resistance of wicks

For an EO pump in series with a saturated wick, the pressure load on the EO pump in Eq. (1) is a function of the hydraulic resistance of the wick as well as the hydrostatic pressure associated with any rise

height. We assume that the wick is completely saturated with liquid water (i.e., operation after a start-up period during which liquid water invades the wick until saturation). As a conservative design assumption, we also assume the pressure gradients in the channels do not significantly influence the flow in the wick (see Litster et al. [8] for further discussion of this effect). The hydraulic resistance of the wick is a function of its porosity, pore diameter, and pore morphology, which are typically lumped into a single permeability parameter. We model pressure-driven flow with negligible inertia in a wick with Darcy's equation:

$$\bar{u} = -\frac{k_w}{\mu_l}\bar{\nabla}p \tag{6}$$

where $\bar{u}$ is the superficial velocity, k_w is the permeability of the wick, and p is the liquid pressure in the wick. Thus, the pressure load of a wick is the sum of hydrostatic and Darcy pressure drops:

$$\Delta p = \rho_l g h + Q_{eo}\frac{\mu_l}{k_w}\left(\frac{L_w}{A_w}\right)_{eff} \tag{7}$$

where h is the rise height, g is the gravitation constant, A_w is the wick's cross-sectional area, L_w is the wick length, and k_w is the permeability of the wick. The ratio of wick length to cross-sectional area will typically be an effective parameter, $(L_w/A_w)_{eff}$, to account for the three-dimensional wick geometry and the distribution of water flux into the wick.

We compute the effective length to area ratio of the porous carbon plate with a three-dimensional finite element solution to Eq. (6) using Comsol Multiphysics 3.3a software. As illustrated in Fig. 2, we specify uniform liquid velocity into the "landing area" of the plate (where it contacts the cathode GDL). The area integral of the liquid water velocity at this interface is set equal to the total water production of the fuel cell (a conservative design approximation). The boundary condition for the outflow of water is a fixed pressure condition at the end of the tab that connects to the pump. The numerical solution was obtained using COMSOL's FGMRES algorithm with 127,485 elements.

Fig. 2 presents the computed liquid pressure distribution on the surface of the porous carbon plate for water production commensurate with operation at 0.5 A cm^{-2}, 100% liquid water production, and a wick permeability of 1×10^{-11} m^2. From the maximum pres-
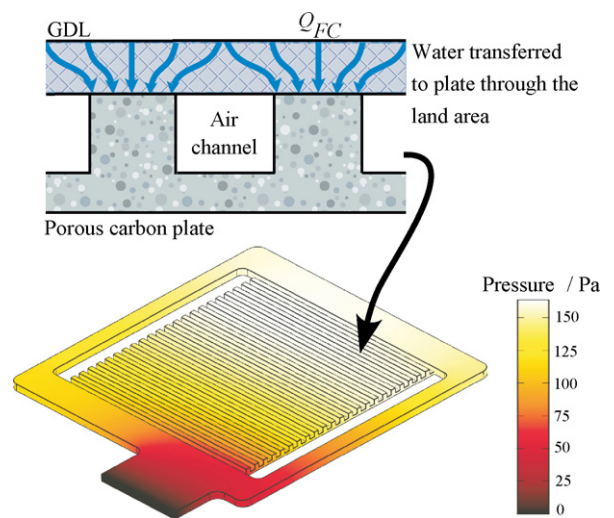

Fig. 2. Pressure distribution in the porous carbon plate for water production consistent with 0.5 A cm^{-2} and an isotropic permeability of 1×10^{-11} m^2. The schematic at the top depicts the specified uniform water flux into the porous carbon plate at the GDL/plate interface (the landing area). We simulate the EO pump on the end of the 2 cm wide tab with a fixed pressure boundary condition (specified as 0 Pa). The liquid pressure gradient increases towards the tab as the volumetric flow rate in the wick increases.

sure difference across the plate (163 Pa), we calculate with Eq. (7) that the effective length to area ratio, $(L_w/A_w)_{eff}$, for the wick is $1400\,m^{-1}$. If a square foot print is maintained, this value of $(L_w/A_w)_{eff}$ is approximately invariant with varying fuel cell area (assuming wick dimensions are much larger than pore diameters). For wicks of fixed out-of-plane thickness, the length of streamlines associated with transport increases proportionally with geometric (in-plane) length; but this increase in length is compensated by a proportional increase of cross-sectional area for transport.

By combining Eqs. (1) and (7) and solving for flow rate, we arrive at an expression for the flow rate of an EO pump in series with a wick having a fixed rise height:

$$Q_{eo} = -\frac{[\varepsilon \zeta V_{eff} f + \rho_l g h a^2/8]}{[\tau \mu_l L/\psi A_{eo} + (a^2/8)(\mu_l/k_w)(L_w/A_w)_{eff}]} \quad (8)$$

From Eq. (8), we can derive a non-dimensional parameter (Θ) for evaluating whether the wick and pump system is flow rate or pressure limited by hydraulic resistance:

$$\Theta = \frac{a^2 \psi A_{eo}}{8 k_w \tau L}\left(\frac{L_w}{A_w}\right)_{eff} \quad (9)$$

If $\Theta \ll 1$, the hydraulic resistance of the wick is insignificant and the pump operates near the maximum flow rate ($Q_{eo} \to Q_{eo,max}$). If $\Theta \gg 1$, the pump's pressure capacity severely restricts the flow rate and the pressure differential across the pump approaches the maximum possible value ($\Delta p \to \Delta p_{max}$). We estimate Θ to be 0.72 for the present system using the representative parameter values in Table 1. In designing such systems, we prefer $\Theta < 1$ in order to maintain reasonably high flow rate per current values and low pump parasitic loads.

Experimental and theoretical analysis by Yao et al. [19] has shown that the maximum thermodynamic efficiency of a porous glass EO pump is achieved when operating the pump at $\Delta p/\Delta p_{max} = 0.5$. However, the key figures of merit for this application are the parasitic load of the EO pump and the ratio of fuel cell volume to EO pump volume (rather than thermodynamic efficiency). In the following section, we assemble a model for evaluating these figures of merit by coupling the EO pump model with an empirical lumped parameter model of a PEM fuel cell.

Table 1
Model parameters for the EO pump model.

Model parameters	Value
Area, A_{eo}	$1.7\,cm^2$
Pump thickness, L	$1\,mm$
Porosity, ψ	0.35
Tortuosity, τ	1.45
Pore diameter, $2a$	$2.0\,\mu m$
pH	3.6
Water relative permittivity, ε_r	78.3
Molar conductivities, $\Lambda_{H_3O^+}, \Lambda_{HCO_3^-}$	350, 44.5 $\mu S\,cm^{-1}\,(mol\,l^{-1})^{-1}$
Water viscosity, μ_l	$0.00089\,Pa\,s$
PVA electrode spacing, δ	$0.6\,mm$
PVA porosity, ψ_{PVA}	0.9
Compressed PVA porosity, $\psi_{PVA,c}$	0.5
Compressed PVA tortuosity, τ_{PVA}	1.45
PVA wick area, A_{PVA}	$0.44\,cm^2$
PVA wick length, L_{PVA}	$2.5\,cm$
PVA permeability, k_{PVA}	$1.0 \times 10^{-10}\,m^2$
Porous carbon permeability, k	$1.0 \times 10^{-11}\,m^2$
$(L_w/A_w)_{eff}$	$1400\,m^{-1}$
EO pump exchange current density, $j_{o,eo}$	$1.8 \times 10^{-5}\,A\,m^{-2}$ [17]
Electrode surface area ratio, r_A	$3.0\,m^2\,m^{-2}$
EO pump Tafel slope, b_{eo}	$0.120\,V$ [18]
EO pump reversible potential, E_{rev}	1.23

2.4. Fuel cell integration and parasitic load

We now incorporate models of the fuel cell's water production and performance in order to identify the minimum pump voltage for complete water removal and evaluate the scaling of the EO pump's parasitic load. Here, we specify that all of the water is produced in liquid form and the EO pump must remove all the water produced by the fuel cell. With Faraday's 1st law of electrolysis, we calculate the fuel cell's volumetric production of water, Q_{FC}, as a function of current density, j_{FC}:

$$Q_{FC} = \frac{M_{H_2O}}{\rho_l}\frac{A_{FC}j_{FC}}{2F} \quad (10)$$

where M_{H_2O} is the molecular mass of water, ρ_l is the density of liquid water, and A_{FC} is the fuel cell area. By equating the expressions for EO pump flow rate and the rate of fuel cell water production, respectively, Eqs. (8) and (10), and assuming negligible rise height, we derive an expression for the minimum effective voltage to remove all product water from the fuel cell:

$$V_{eff} = -\frac{\mu_l}{\varepsilon}\underbrace{\left[\frac{M_{H_2O}j_{FC}}{2\rho_l F}\right]}_{\text{Water production}}\underbrace{\left[\frac{A_{FC}}{A_{eo}}L\right]}_{\text{Geometry}}\underbrace{\left[\frac{\tau}{\psi \zeta f}\right]}_{\text{Substrate}}\underbrace{\left[1+\Theta\right]}_{\text{Resistance}} \quad (11)$$

As labeled, Eq. (11) contains four major groupings of parameters relating to the rate of water production, the geometry of the fuel cell and pump, the pump substrate material, and the relative influence of the wick's hydraulic resistance. Eq. (11) has several implications. As current density increases, water production increases, and the minimum voltage requirement for complete water removal increases proportionally. In addition, the ratio of fuel cell area to EO pump area has a proportional effect on the voltage requirement. The required voltage also increases proportionally with pump substrate thickness and tortuosity, but scales inversely with porosity and zeta potential.

The parasitic load of the EO pump, P_{eo}/P_{FC}, is a key figure of merit for this system and is expressed as

$$\frac{P_{eo}}{P_{FC}} = \frac{I_{eo}V_{app}}{A_{FC}j_{FC}V_{FC}} \quad (12)$$

where we estimate the necessary V_{app} from the minimum required effective voltage, V_{eff}, using Eq. (4). The pump current in Eq. (12), I_{eo}, is a combination of electromigration, EO advective current, and pressure-driven advective current. Yao and Santiago [11] offer the following expression for the current associated with EO flow in porous media at the maximum flow rate condition ($\Delta p = 0$):

$$I_{max} = \frac{\psi}{\tau}\frac{f\sigma_\infty}{g}\frac{A_{eo}}{L}V_{eff} \quad (13)$$

With a pressure load, the total current of the EO pump is the current for maximum flow rate plus the advective current generated by pressure-driven flow, $I_{\Delta p}$:

$$I_{eo} = I_{max} + I_{\Delta p} \quad (14)$$

The expression for the pressure-driven advective current is [11]:

$$I_{\Delta p} = \frac{\psi}{\tau}A_{eo}\frac{\varepsilon \zeta f}{\mu}\frac{\Delta p}{L} \quad (15)$$

Pressure-driven advective current is often neglected in predictions of EO pump current because of the higher conductivity of the commonly used buffer solutions [19]. However, in fuel cell applications, there is the possibility for significant pressure-driven advective current when pumping low ion density water with pressure loads near the pump's maximum pressure. Perhaps counter-intuitively, the current generated by an adverse pressure gradient (i.e., a pressure load) acts to reduce the total current and power consumed by the EO pump (for a given applied voltage).

For fuel cell water removal applications, we hypothesize that the EO pump generates an additional, internal pressure load when the applied voltage is greater than that necessary to remove water from the fuel cell at steady-state. The induced pressure load and the corresponding reverse pressure-driven flow serve to balance the difference between the nominal EO pump flow rate and the steady-state water production of the fuel cell (i.e., to satisfy conservation of mass). The capillary pressures associated with the porous regions between the pump electrodes sustains the additional pressure load (i.e., the pump is "attempting" to pump itself dry but cannot due to capillary forces). The induced pressure-driven flow rate is the difference between the volumetric water production of the fuel cell and the EO flow rate, if there is an infinite reservoir of water, Q_{eo}^*. With excess applied voltage, the total pressure differential across the pump in Eqs. (1) and (15) can be expressed as

$$\Delta p = \rho_l g h + Q_{eo} \frac{\mu_l}{k_w} \left(\frac{L_w}{A_w} \right)_{eff} + 8 \frac{\tau}{\psi} \frac{\mu_l L}{a^2} \frac{(Q_{eo}^* - Q_{FC})}{A_{eo}} \tag{16}$$

To determine parasitic load with Eq. (12), we use an empirical lumped parameter model [3] to predict fuel cell voltage at a given current density:

$$V_{FC} = E_{rev} - R j_{FC} - b \ln \left(\frac{j_{FC}}{j_o} \right) - c \ln \left(\frac{j_L}{j_L - j_{FC}} \right) \tag{17}$$

The first term on the RHS of Eq. (17), E_{rev}, is the reversible potential of the fuel cell at open circuit conditions. The second term is the Ohmic overpotential where R is the area specific resistance. The third term is the activation overpotential in which b and j_o are the effective Tafel slope and exchange current density, respectively. The last term is the mass transfer overpotential where c is an empirically determined constant and j_L is the limiting current density. Eq. (17) is not a comprehensive model, but is sufficient for predicting the parasitic load of the pump without the ambiguities and complexities of more advanced fuel cell models.

2.5. Water conductivity and zeta potential versus pH

EO pumps are typically operated with buffer solutions in order to maintain the solution pH at optimum levels [15,19–21]. The buffer is typically selected so that its pH is significantly higher or lower than the isoelectric point of the pumping substrate (the solution pH at which the surface has zero charge) [22]. When pumping unbuffered water with an EO pump, as in a fuel cell, the pH of the water decreases significantly due to the production of H_3O^+ ions at the anode (from the oxygen evolution reaction). In this work, we account for reduced pH with expressions relating pH to ionic conductivity and zeta potential. We assume that the hydronium ions, H_3O^+, are charge-balanced by bicarbonate, HCO_3^-, because these are the primary ions expected from the dissolution of carbon dioxide from the atmosphere (CO_2 dissolves into and reacts with water to form carbonic acid, H_2CO_3, which then dissociates and reacts with water to form H_3O^+ and HCO_3^-). As the mobility of hydronium is very high relative to possible counter-ions, the counter-ion identity is less crucial for engineering estimates. We estimate conductivity at a given pH using the equation:

$$\sigma_\infty = 10^3 (\Lambda_{H_3O^+} + \Lambda_{HCO_3^-}) 10^{pH} \tag{18}$$

where $\Lambda_{H_3O^+}$ and $\Lambda_{HCO_3^-}$ are the molar conductivities.

The zeta potential generated at the glass/liquid interface is a strong function of pH [22]. The absolute value of the zeta potential of borosilicate glass in contact with water decreases with lowering pH since the isoelectric point of glass is ~2.8 [22]. If the pH decreases towards 2.8, the zeta potential tends to zero and no EO flow can be generated. In this work, we use an empirical correlation from Yao and Santiago [11] to generate a scaling for zeta potential versus pH

based on reference values of zeta potential, ζ_{ref}, and pH, pH_{ref}:

$$\zeta = \zeta_{ref} \left(\frac{0.026 - 0.058 \ \log_{10}(pH)}{0.026 - 0.058 \ \log_{10}(pH_{ref})} \right) \tag{19}$$

For the present model, we use a reference zeta potential and pH of -64 mV and 5.2, respectively [15]. Fig. 3 presents the prescribed dependencies of conductivity and zeta potential on the pH of water exposed to CO_2. The plot of zeta potential illustrates the significant reduction in zeta potential as pH tends toward the isoelectric point. Fig. 3 also contains a plot of the factor g versus pH (g being the non-dimensional parameter related to finite EDL effects on flow rate per current [11,15]). g increases at low pH as the EDL compresses with higher concentrations of hydronium and bicarbonate, causing the EO velocity profile to become increasingly flat.

The combined influence of pH on the conductivity, zeta potential, and EDLs has a strong effect on the ratio of maximum flow rate to current:

$$\frac{Q_{eo,max}}{I_{eo,max}} = \frac{g}{\sigma_\infty} \frac{\varepsilon \varsigma}{\mu_l} \tag{20}$$

As Fig. 3 shows, Q_{eo}/I_{eo} decreases by three orders of magnitude as the pH is reduced from 5.5 to 3. The ratio of flow rate per current provides a useful indication of pH change in the porous glass. When EO pumping DI water in conventional EO pumps with large reservoirs [15,19], we commonly measure decays in maximum flow rate per current down to $\sim$0.2 ml min^{-1} mA^{-1}. That flow rate per current is consistent with our measurements of the pH decreasing to 4. In estimating the performance of smaller EO pumps in series with wicks, we specify a pH of 3.6. This pH agrees with direct measurements (using pH paper by EMD Chemicals, Inc., Darmstadt, Germany, with a resolution of approximately 0.2 pH units) which we have obtained from water extracted from the PVA sponge between the Pt mesh and the porous glass. We have also observed that the region of decreased pH was confined to within about 1 mm of the region bounded by the pump's electrodes. We found no significant pH changes in the wick. We hypothesize that the advection and electromigration fields dominate the effects of upstream diffusion. The two main implications of Fig. 3 are that the pump's parasitic load increases and its pressure capacity decreases at low pH because of greater conductivity and lower zeta potential, respectively.
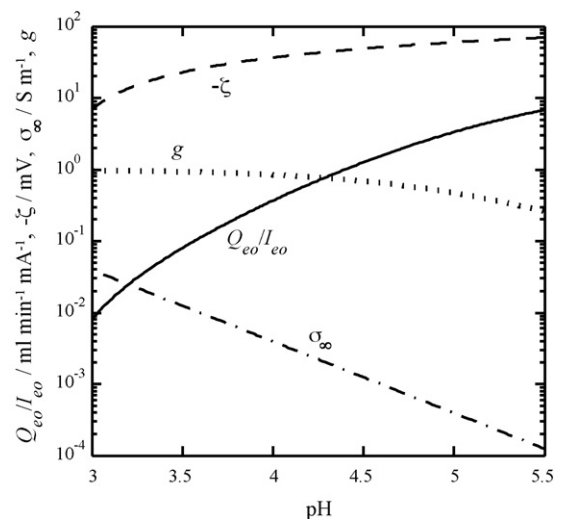

Fig. 3. Influence of water pH on the ratio of maximum flow rate per current, Q_{eo}/I_{eo}, zeta potential, ζ, bulk water conductivity, σ_∞, and the non-dimensional effect of the EDL on flow rate per current, g, for a 2 μm pore diameter. The reduction of pH from 5.5 to 3.6 (due to H_3O^+ production at the anode) results in a two-order of magnitude reduction in flow rate per current.

Table 2
Empirical values used for the lumped parameter fuel cell model. The parameters, b, j_o, and c were extracted from the polarization curve in Ref. [8] for an air stoichiometric ratio of 1.3 and an applied EO pump voltage of 12 V. The R^2 value of the fit was 0.999. The area specific resistance, R, is the experimental measurement.

Parameter	Value
E_{rev}	1.2 V
R	0.17 Ω cm^2
b	0.0506 V
j_o	7.1×10^{-5} A cm^{-2}
c	0.0619 V
j_L	1.1 A cm^{-2}

2.6. EO pump parasitic power dependence on fuel cell operation

We now use the model described above to provide an estimate of EO pump parasitic load versus fuel cell polarization and the influence of the three key length scales of the EO pump (pore diameter, thickness, and area). Table 1 lists the parameter values used to model the wick and EO pump system. Table 2 lists the empirical parameters for the fuel cell model. The values are consistent with the experimental setup in this paper and in Ref. [8].

Fig. 4 presents three curves of parasitic EO pump load versus fuel cell current density and the polarization curve from the empirical fuel cell model. The two theoretical parasitic load curves are for cases with (1) a constant applied EO pump voltage of 12 V, and (2) the minimum voltage to remove all product water as determined by Eq. (11). As Fig. 4 shows, the predicted parasitic load of the EO pump is below 2% over the majority of current densities in both cases. At moderate current densities, the parasitic load is below 0.5%. These results suggest that large reductions in parasitic load are possible if the minimum required pump voltage is used at each current density rather than a high voltage that offers robust performance at all current densities. Furthermore, we note that the parasitic load of the EO pump tends to zero as current density approaches zero, which is a desirable characteristic. This is in contrast to the percent parasitic load of air delivery in automotive systems at low currents, which can approach 100% [23].
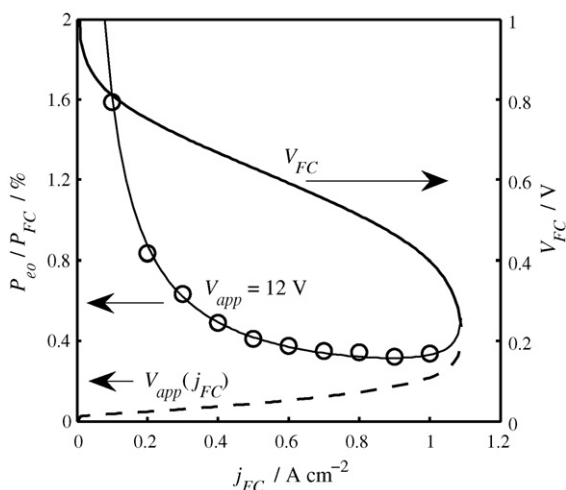

Fig. 4. Predictions of EO pump parasitic load, P_{eo}/P_{FC}, versus fuel cell current density, j_{FC}. Parasitic load curves (pump power over fuel cell gross power) are plotted for a constant applied EO pump voltage of 12 V, V_{app} = 12 V (—), and with minimum voltage for complete water removal, $V_{app}(j_{FC})$ (–). The scale for the polarization curve, V_{FC}, is shown on the right axis. The corresponding experimental measurements (○) of parasitic load at V_{app} = 12 V from ref. [8] are plotted for comparison. The curve for parasitic load with the minimum applied voltage for water removal, $V_{app}(j_{FC})$, presents a theoretical lower bound to the parasitic load.
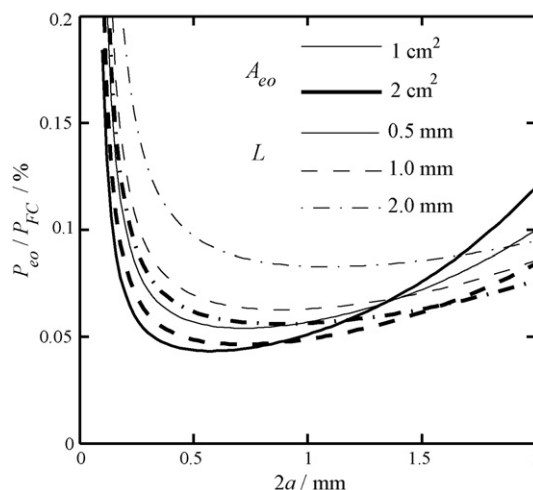

Fig. 5. Theoretical EO pump parasitic load versus pore diameter when the 25 cm^2 fuel cell operates at a current density of 0.5 A cm^{-2} and an air stoichiometric ratio of 1.3. We plot curves for 1 cm^2 (thin lines) and 2 cm^2 (thick lines) EO pumps with substrate thicknesses of 0.5 (—), 1.0 (- - -), and 2.0 (- –) mm. We estimate EO pump power based on the minimum effective voltage requirement for complete water removal. Optimum pore diameters are between 0.5 and 1 μm.

In Fig. 5, we present curves of parasitic load versus pore diameter to illustrate the scaling of the EO pump parasitic load versus the three key length scales of the EO pump (pore diameter, thickness, and area). First, we comment on the effect of pump pore diameter. The model shows that pore diameter (the geometric feature most difficult to vary experimentally) has the strongest effect on system performance. The curves indicate that pore diameters between 0.5 and 1 μm result in near minimum parasitic losses. If the pore diameter is too large, the pump requires high voltages to meet the pressure load requirements (maximum pressure scales as $\Delta p_{max} \propto V_{eff}/a^2$), while pump power scales as the product $V_{eff}V_{app}$. However, parasitic load also increases if the pore diameter is too small due to the effect of the finite EDL thickness (low values of the parameter f [11]).

Second, we comment on the effect of pump thickness. Minimum parasitic loads are for approximately 0.5 mm thick substrates. Thicker pumps require more voltage (and power) to generate the same electric field, V_{eff}/L, and flow rate. Conversely, thinner pumps result in low pump resistance relative to the resistance associated with electrode spacing, δ, which decreases the effective voltage, V_{eff}, relative to the applied voltage. Since maximum pressure is proportional to V_{eff}, decreasing substrate thickness results in lower pressure capacity.

Third, we comment on the effect of pump area versus pore diameter. If the pore diameter is well matched to the pressure load (i.e., the EO pump operates far from the maximum pressure condition), the parasitic load decreases with larger areas because a lower EO velocity can meet the flow rate demand. However, if the pores are larger than ideal (e.g., 2 μm), parasitic loads for water removal can increase with increasing pump area. This is because there is a minimum voltage to meet pressure load requirements and at a fixed voltage the power scales proportionally with area.

A significant result shown in Fig. 5 is that the EO pump's parasitic load is below 1% over the entire range of the parameters plotted. Thus, even a significantly less than optimum pump can meet water removal requirements with minimal parasitic load. Alternatively, a well-optimized pump's volume can be very small relative to the fuel cell and still be a negligible parasitic loss.

With the theoretical model, we have developed a general, conservative guideline for sizing EO pumps to fuel cells. To maintain a parasitic load below 1%, the ratio of fuel cell active area to EO pump area should be 100 or less. This is a fortuitous result, as a simple

Table 3
Experimental fuel cell operating conditions.

Parameter	Value
Endplate temperatures	55 °C
Air and hydrogen dew points	55 °C
Gas line temperatures	60 °C
Air and hydrogen outlet pressures	Ambient
Air stoichiometric ratio	1.5
Hydrogen stoichiometric ratio	2.0

geometric analysis reveals there is typically enough planar area on a single side of a square stack (with a unit cell pitch of 2 mm) to achieve this ratio. We therefore hypothesize that this technology is scalable to stacks with minimal volume addition and parasitic loads below 1%.

3. Experimental

We here provide a brief summary of the fuel cell design, fabrication, and the experimental apparatus as they are identical to the 25 cm^2 fuel cell used and discussed in detail by Litster et al. [8]. The cathode flow field plate features an internal porous carbon wick and an external EO pump, as shown in Fig. 1. The cathode plate has a strictly parallel channel architecture with 23 channels that are 1.0 mm deep and 1.2 mm wide. The width of the ribs is 1.0 mm. The flow field is machined into a porous carbon plate (SGL SIGRACET-plate PGP material, SGL Carbon AG, Germany). We embed the wick into a machined graphite plate for support and sealing. The EO pump has a porous borosilicate substrate (Robu-Glas, Germany) with a 2 cm^2 area and a thickness of 1 mm. The porosity is approximately 35% (from wet/dry measurements) and the mean pore diameter is 2 μm. A dielectric wick made of polyvinyl alcohol (PVA) sponge (PVA Unlimited, Warsaw, IN) connects the EO pump to the porous carbon and insulates the fuel cell from the EO pump (i.e., the high electrical resistance of the water-saturated PVA prevents significant current from passing between the EO pump and the fuel cell). The EO pump electrodes are platinum mesh (Goodfellow Cambridge Limited, UK). The graphite anode flow field plate features three serpentine channels 0.75 mm deep and 0.75 mm wide with a rib width of 0.75 mm. The MEA (Ion Power, Newcastle, DE) features a catalyst-coated membrane with a 25 μm thick Nafion membrane and a platinum loading of 0.3 mg Pt cm^{-2}. We sandwich the MEA between SGL-SIGRACET 10-BB GDLs (Ion Power).

We operate the fuel cell in series with a four-wire DC load (Agilent N3100A, Palo Alto, CA) and a boost power supply (Acopian W3.3MT65, Easton, PA). Mass flow controllers (Alicat Scientific, Tucson, AZ) regulate gas flow rate and a dew point control system (Bekktech LLC, Loveland, CO) controls the gas dew points and the temperatures of the cathode end plate and the heated lines (Clayborn Labs, Inc., Truckee, CA). A second temperature controller (Omega Engineering, Inc., Stamford, CT) controls the anode end plate temperature. A separate power supply (Agilent 6030A DC electronic load) applies a constant voltage to the EO pump and we measure current by the voltage drop over a 28 Ω resistor in series with the EO pump. In the experiments, the gases are fully humidified and a high hydrogen stoichiometric ratio of 2.0 is used to ensure that observations of flooding are restricted to cathode phenomena. Table 3 lists the rest of the fuel cell operating conditions.

4. Results and discussion

We now present experimental studies with three major objectives. First, we use the experimental results to evaluate the theoretical model's predictive capabilities. Second, we use a comparison between *ex situ* experiments and *in situ* experiments to

study the effects of an integrated wick and the fuel cell's finite water supply on EO pump operation. Third, we use parametric studies of applied EO pump voltage to analyze the relationship between water removal rate and flooding prevention. These findings have utility beyond the present system because they offer insight for the design of alternative water management systems.

4.1. Ex situ EO pump characterization

Ex situ measurements of the EO pump's performance were made to verify the theoretical model, assess the performance of an EO pump with an integrated wick, and provide a reference for EO pump performance when later integrated with a fuel cell. The reference performance of the EO pump is useful as the pump operates with finite water supply when integrated with the fuel cell (i.e., the steady-state flow rate can only be as high as the rate of water production). This operating mode has not previously been investigated. Thus, this *ex situ* experiment is a control case for the *in situ* measurements.

We made our *ex situ* measurements with the same EO pump that we integrated with the fuel cell. Instead of the porous carbon plate, a 2 cm wide and 2.2 mm thick PVA wick was connected to the EO pump. The end of the wick was placed in a bath of DI water with a rise height of 1 cm and a wick length of 2.5 cm. We measured the flow rate of the EO pump by effluent weighing with a microbalance (ACCULAB, Newtown, PA, USA) placed underneath the EO pump. Fig. 6a presents a schematic of this experimental setup. We obtained measurements by consecutively dwelling at each voltage, ranging from 6 to 40 V, for 10 min. We report the mean values over each 10 min dwell period.

Fig. 6b presents the flow rates measured by weighing effluent water as a function of EO pump power. We also plot the flow rate predicted by Eq. (8) with an empirically determined PVA wick permeability of 1.0×10^{-10} m^2. For this wick, the hydraulic resistance parameter, Θ, is 0.034, indicating that the pump flow rate should not be hindered by the wick's hydraulic resistance (cf. Section 2.3). The measured mean flow rate per current ratio was order 0.1 ml min^{-1} mA^{-1}, which is consistent with a mean pH of 3.6 (the prescribed pH value for the model predictions in this work). We observe good agreement between the measured and predicted flow rate curves. The data shows that the wick and pump architecture do not introduce unexpected hindrances to the performance of the EO pump, provided there is an excess supply of water.

For reference, Fig. 6b outlines a region of desired EO pump operation when integrated with the fuel cell. In this area, the EO pump consumes less than 1% of the fuel cell power at 0.5 A cm^{-2} and the pump's flow rate is equal to the water production rate at 0.5 A cm^{-2} or greater (assuming 100% liquid phase water). In the *ex situ* experiments, the pump consistently met these requirements with applied voltages ranging from 6 to 20 V.

4.2. Fuel cell flooding prevention

We now present *in situ* experimental results where we apply a constant voltage to the EO pump to prevent flooding in an operating fuel cell. These results allow us to investigate the relationship between applied voltage and fuel cell performance, as well as the EO pump's flow rate and parasitic load. We compare these results with our theoretical model.

The *in situ* experiments were performed with the fuel cell operating at a current density of 0.5 A cm^{-2} and an air stoichiometric ratio of 1.5 over a 40 min period. We performed multiple realizations with EO pump voltages ranging from 0 to 40 V. These results are useful for identifying a minimum EO pump voltage to prevent flooding. There are many potential advantages to running the EO pump with the lowest possible voltages, including a lower para-
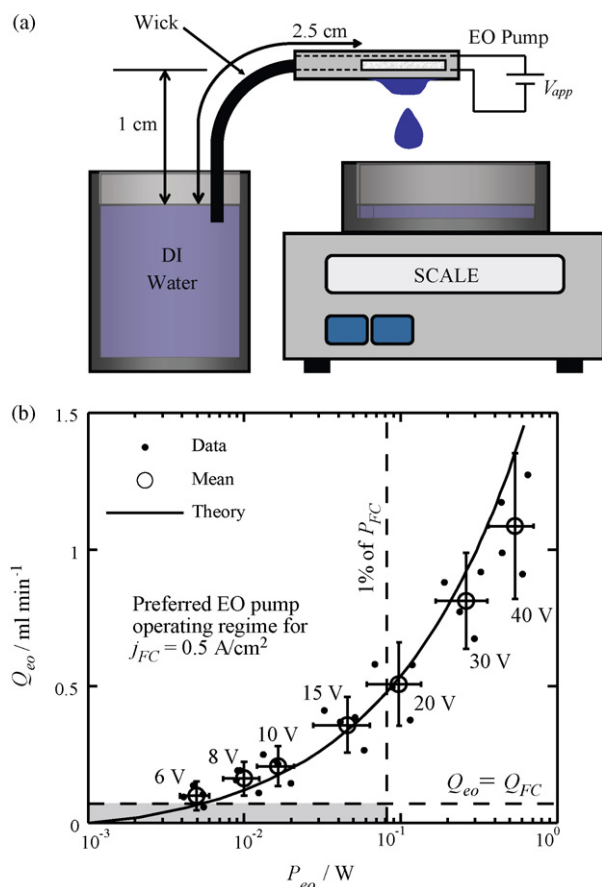
Fig. 6. (a) Experimental setup for *ex situ* testing of the EO pump attached to a PVA wick. (b) Flow rate versus the power consumed by the EO pump. The unshaded region is the preferred operating regime for the EO pump when integrated with a fuel cell operating at 0.5 A cm^{-2} (complete water removal and a parasitic load of less than 1%). We find this condition is met with voltages between 6 and 20 V. The error bars represent 95% confidence intervals for the mean value determined from four realizations.

sitic load and less electrolytic current to generate bubbles and pH changes.

Fig. 7 presents a representative set of fuel cell voltage time-series with applied EO pump voltages between 0 and 6 V. Between each realization, we disassembled the EO pump and rinsed it in DI water to ensure consistent initial water pH in the pump. Before the beginning of each time series, the fuel cell air channels were purged at a flow rate of 2000 sccm for 5 s for an initial flooding-free condition. We filtered the time series by convolving the data with a Gaussian kernel with a 250 ms standard deviation (approximate residence time of air in the channels), which negligibly affects the physical trends observed. The transients in this figure show a consistent increase in fuel cell voltage as EO pump voltage increases to 5 V. At 5 V, EO pumping yielded a 14% increase in fuel cell power and stabilized the performance (note the suppression of sharp intermittent voltage drops which we associate with channel flooding). Applied voltages above 5 V did not significantly improve performance. Thus, we identify that V_{app} = 5 V was the minimum EO pump voltage to stabilize the fuel cell's performance for this operating condition.

4.2.1. EO pump flow rate

Next, we compare the water pumped by the electroosmotic pump to the gross total flow rate of water (liquid and vapor) produced by the fuel cell. As we shall see, the EO pump has to pump only roughly half the total water produced to prevent flooding. Fig. 8a presents the flow rate of the EO pump for 17 experiments in which

the applied pump voltage was varied between 3 and 40 V. We measured the flow rate by collecting the pump effluent in a slender (to minimize evaporation) 5 ml graduated cylinder. The water was collected over the last 30 of the 40 min experiments (from 10 to 40 min in Fig. 7) in order to record an approximately steady-state measurement. We present the flow rate of liquid water as a percentage of the total amount of water produced (70 µl min^{-1} at 0.5 A cm^{-2} if all product water is liquid). In our experiments, 3 V was the lowest applied voltage for which we could obtain a measurable flow rate. This is consistent with 3 V being close to the voltage of water decomposition (2.5 V from Eq. (3)).

As we expect, at low applied voltages (less than 5 V), the flow rate varies approximately linearly with applied voltage. To highlight this region, we show the data with the predicted linear flow rate dependence which follows from Eq. (8). However, the agreement between the data and model worsens above 5 V. At the minimum applied voltage that prevented flooding (V_{app} = 5 V), the EO pump removed 36% of the gross product water. At applied voltages above about 12 V, the flow rate of liquid water through the pump reached a plateau at a maximum value of approximately 53% (37 µl min^{-1}). We highlight the plateau in the figure with a dashed horizontal line. We discuss possible causes for this plateau in Section 5 below.

Fig. 8b shows a plot of the measured fuel cell voltage averaged over the period from 30 to 40 min (i.e. representative, steady-state voltage) versus the percent of water removed by the EO pump. First, as a basis for comparison, we show fuel cell voltage with zero applied pump voltage. With the EO pump off, V_{app} = 0 V, the mean steady-state fuel cell voltage over four realizations was 0.58 V with a standard deviation of 20 mV. For comparison, we show this mean and standard deviation with solid and dashed lines, respectively. With regard to the experimental variation of applied pump voltage, we measured a consistent increase in the steady-state fuel cell voltage with greater water removal rates. For water removal rates at or below which flooding is prevented (Q_{eo}/Q_{FC} = 38%), we see that fuel cell voltage follows a roughly linear relationship (R^2 = 0.93). Above this, fuel cell voltage shows a much weaker dependence on percentage water removed. These data suggests the fuel cell performance is free of flooding for water removal rates greater than 38%.
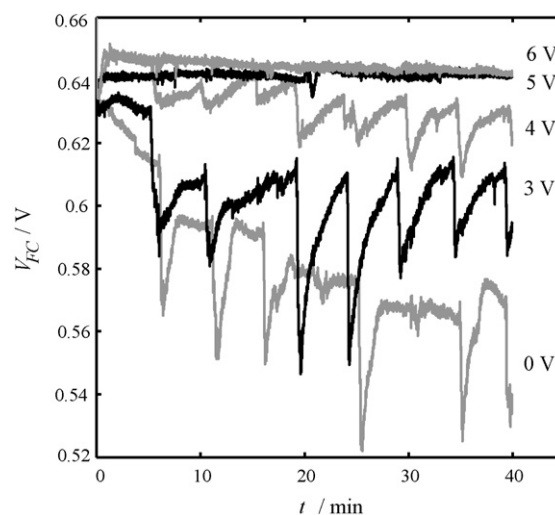

Fig. 7. Transient fuel cell voltage at 0.5 A cm^{-2} for EO pump voltages ranging from 0 to 6 V. The air stoichiometric ratio was 1.3. With zero applied pump voltage, there were large voltage fluctuations and significant overall decay of the fuel cell voltage. With higher applied pump voltage, the rate of decay and the magnitude of the voltage instabilities decreased. Above an applied voltage of 5 V, there were only marginal increases in fuel cell voltage with greater EO pump voltage.
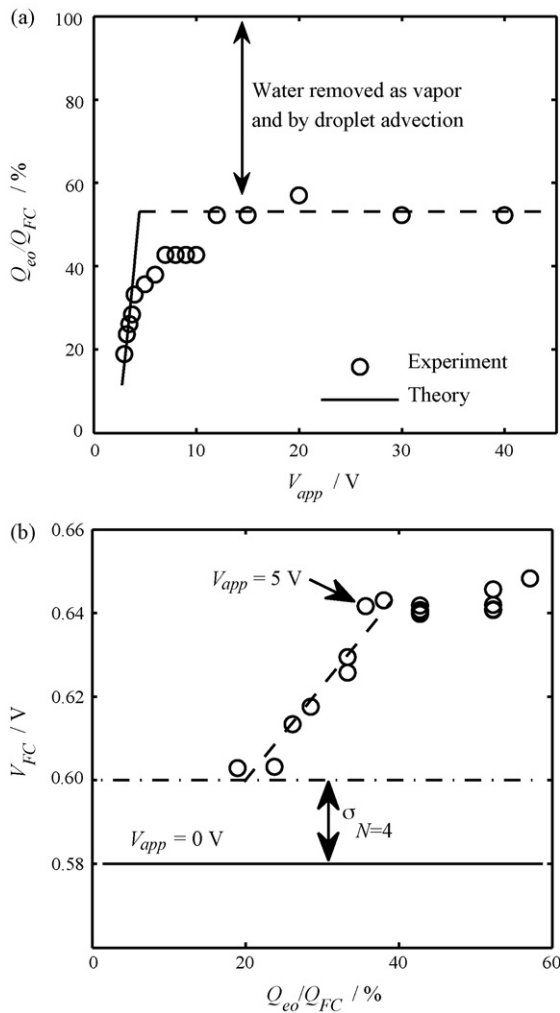
Fig. 9. Initial transients of EO pump current at applied voltages of 3, 5, and 12 V. With a low voltage of 3 V, the current is relatively steady after initial startup. With 5 V, the current increases with decreasing pH (increasing conductivity) in the porous glass and reaches a steady-state. With a high voltage of 12 V, the current increases more rapidly with pH decrease, then decays due to capillary drainage of the PVA. This decay in current is responsible for the plateau in the current versus voltage results in Fig. 10a.

Fig. 8. (a) EO pump flow rate versus applied voltage. The flow rate is normalized by the total water production, assuming 100% liquid water production (Q_{FC} = 70 μl min^{-1}). The solid line is the theoretical prediction of the flow rate, Eq. (8), and the dashed line is the mean normalized flow rate of 53% in the plateau region (voltages of 12 V and greater). (b) Steady-state fuel cell voltage versus normalized EO pump flow rate. The dashed line (–) is a linear fit to the linear region of increasing fuel cell voltage with increasing EO pump flow rate. The horizontal solid line (–) is the mean steady-state fuel cell voltage from four realizations with the EO pump off (Q_{eo}/Q_{FC} = 0). The horizontal dash-dot (- – -) lines indicate the standard deviation of the steady-state voltage when the EO pump is off.

sitic load remains below 2% with applied voltages as high as 40 V. These results illustrate the negligible parasitic load of EO pumping and support the favorable scaling of EO pumps with fuel cells that the model suggests. However, we note that at applied voltages above 5 V, there is significant discrepancy between the model and measurements. This discrepancy is discussed in the next section.

Fig. 10. Current (a) and parasitic load (b) of the EO pump. The current versus applied voltage deviates from the theoretical linear behavior due to decreasing pH with increasing currents and capillary drainage of the PVA at high voltages. The dashed portion of the theoretical curves are ranges at which we have low confidence in the model because of capillary drainage. With applied voltages below 20 V, the parasitic load is below 1%. The minimum parasitic load necessary to prevent flooding is 0.07% at an applied voltage of 5 V.

4.2.2. EO pump current and power

Fig. 9 shows representative initial transient measurements of current at applied pump voltages of 3, 5, and 12 V. The trends in transient current measurements differ with the magnitude of V_{app}. At very low voltages (3 V), our instantaneous current measurements are uniform over nearly the entire duration. At moderate voltages (5 V), the current increased over the first 2 min and then leveled off to a steady-state value. At higher voltages (12 V), the current measurements increased sharply at first, peaked, and then decayed to a lower voltage. We discuss our hypothesis for the cause of these trends in the times series in Section 5.

Fig. 10a presents the steady-state current drawn by the EO pump versus the applied voltage and compares it with the model prediction. At applied voltages less than 8 V, the current measured varied linearly with EO pump voltage, as expected from theory. As shown in Fig. 10b, at the minimum voltage to prevent flooding, 5 V, the parasitic load of the EO pump is 0.07%. Further, the para-
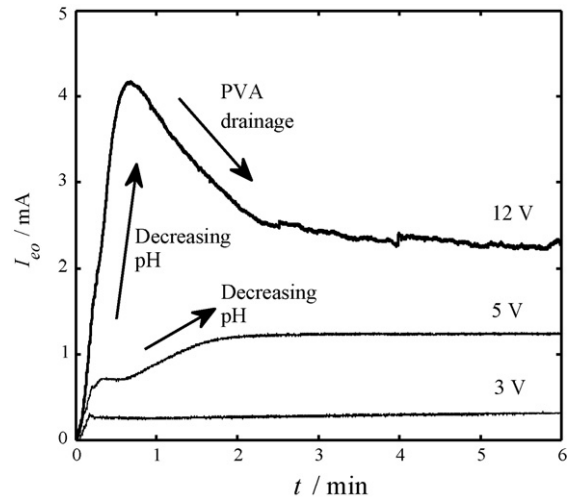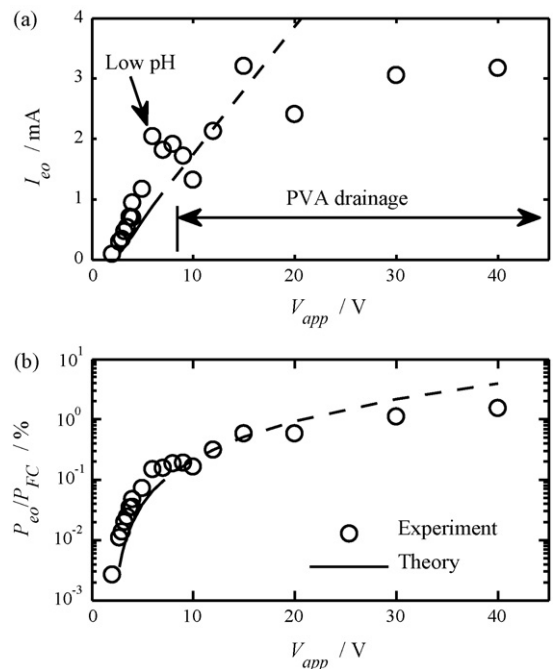
5. Further discussion

As discussed above, the model predicts trends in pump flow rate, current and power fairly well up to about $V_{app} = 5\,V$; the minimum pump voltage to prevent flooding. The model is therefore an effective engineering tool in designing and predicting pump characteristics for low parasitic power cases. However, there were a number of deviations between the model and the experimental results, particularly at higher applied pump voltages. The differences include: (1) the maximum EO pump flow rate being significantly less than the production rate; (2) the non-linear flow rate versus pump voltage data at applied voltages between 5 and 12 V; and (3) a respective over- and under-prediction of EO pump current at low and high applied voltages. We here discuss these discrepancies and elaborate further on the linear relationship between fuel cell voltage and the EO pump flow rate at water removal rates below that required to prevent flooding.

Several factors contribute to the flow rate plateauing at 53% of the water production rate rather than reaching 100% (see Fig. 8a). First, with an expected 3 °C increase in temperature in the channels due to internal heating [24], we calculate that at least 15% of the product water is removed as vapor in the air and hydrogen exhaust. Second, our mass transfer estimates suggest that water evaporation from the exposed EO pump surfaces may account for up to 5% of the product water (assuming a maximum Sherwood number of 100). We therefore estimate that a remaining ∼30% of the product water leaves the fuel cell as liquid in the anode and cathode exhaust gases.

We attribute the linear relationship between water removal rate and increased fuel cell voltage (Fig. 8b) to the spatial-dependence of clearing liquid water from clogged channels at lower voltages. This hypothesis is based partly on current distribution measurements performed on this system with a segmented anode plate (see Ref. [10]). That study showed that the EO pump preferentially pulls water from regions of the wick nearest to the EO pump because of the hydraulic resistance's dependence on the flow lengths in the plane of the cell (i.e., the pressure load for removing water close to the pump is lower). Thus, as voltage increases, the EO pump is able to remove water from regions progressively further away and clear channels that flood at lower voltages.

We now discuss the cause for the steady-state EO pump current measurements being greater than the model's predictions at applied voltages between 5 and 10 V (see Fig. 10a). As Fig. 9 shows, 30 s after activating the pump with an applied voltage of 5 V the current increases over a 2 min period. This transient increase is of the same magnitude as the difference between the model prediction and the steady-state experimental measurement. We attribute this higher than predicted current measurements and the initial transient increase in current to the effect of decreasing pH (and increasing conductivity) in the pump. The oxygen evolution reaction at the anode (pump inlet) introduces hydronium ions, lowering pH. We verified the decrease of pH by dissembling the EO pump after experiments and squeezing water out of the PVA to measure its pH with pH paper strips. The pH values varied between about 5–3.5 with applied voltages between 4 and 40 V (the lowest pH values were observed at the highest voltages). However, these approximate pH measurements are likely higher than the *in situ* values because of mixing and dilution while the pump is disassembled and water samples extracted. Note the flow rate through the pump is reduced relative to the *ex situ* experiments of Section 4.1 because of the greater hydraulic load imposed on the pump by the porous carbon wick. This causes an increase in production of H_3O^+ relative to pump flow rate, and yields lower pH and higher conductivity.

At high applied voltages (>20 V), the current measurements of Fig. 10a are less than model predictions. We attribute this to the finite availability of water to the EO pump and the resulting drainage of the PVA in the pump. The drainage occurs as the pressure capac-ity of the pump (proportional to voltage) approaches the capillary pressure in the wick. We measured the rise height of water in the PVA to be 8 cm, which corresponds to a capillary pressure of approximately 800 Pa. For comparison, 850 Pa is the estimated maximum pressure of the EO pump with an applied voltage of 10 V. Thus, at voltages approaching 10 V and higher, the EO pump is capable of draining the PVA. In Fig. 9, the decay of the current with an applied voltage of 12 V suggests drainage occurs over a 2 min period during initial operation (the PVA is initially saturated at $t = 0$). When the PVA is drained, the cross-sectional area for ionic conduction decreases (ionic resistance increases) and current decreases. We have confirmed this drainage effect with on-going experiments on the coupling of EO pumps with wicks, which we will report in a future publication.

Next, we comment on the non-linearity of the EO pump flow rate data as shown in Fig. 8a. We hypothesize that the effects of decreasing pH and PVA drainage act in concert to generate the deviation from the linear theoretical prediction in Fig. 8a. Decreasing pH increases EO pump parasitic load (due to higher conductivity) and also reduces flow rate because of the reduction in zeta potential at lower levels of pH. Further, the reduction in PVA liquid saturation (and associated lowering of its ionic conductance) causes a greater portion of the applied voltage to be dropped across the anode-to-pump wick space; reducing the effective voltage dropped across the pump and reducing flow rate. Thus, we identify that maintaining higher levels of pH and minimizing the drainage of the intermediate wick (the dielectric PVA) are important system features to address in future work.

To sum up, our experimental results and model predictions indicate an external EO pump coupled to an integrated wick is able to prevent flooding in a PEM fuel cell with negligible parasitic loads. Our study on the effect of applied EO pump voltage supports a conservative guideline (developed with scaling from the model) that a parasitic load of less than 1% can be maintained by using an EO pump with an area that is 0.01 of the fuel cell active area or greater (for all scales of fuel cells). The area ratio in our experiment was 0.08 and the minimum parasitic load to prevent voltage loss due to flooding was 0.07%. This same theoretical scaling suggests that parasitic load would be roughly 0.5% if the EO pump area was 0.01 of the fuel cell area (e.g., a 5 mm × 5 mm pump area). Our current research efforts are addressing the maintenance of the pH in the pump and the use of EO pumps to drain the internal wicks. The use of EO pumps to drain the fuel cell and wicks may open the potential for novel freeze protection strategies when operating in sub-zero environments [25,26].

6. Conclusion

We presented an investigation of flooding prevention in PEM fuel cells with the use of integrated wicks and EO pumps. We presented a theoretical model that elucidates the scaling of EO pumps with fuel cells. The model extends our previous EO pump models to account for additional factors significant to this application, including the hydraulic resistance of the wicks, induced pressure-driven advective current, variation of water pH with electrolysis, and the pump's electrochemical reactions. We verified the accuracy and limitations of this model with both *ex situ* and *in situ* fuel cell experiments. The model results indicate favorable scaling between EO pumps and fuel cells. From the theoretical scaling, we conservatively suggest that parasitic loads below 1% are possible for fuel cell stacks of all sizes as long as the EO pump area is 1% of the fuel cell active area or greater.

The model provides reasonable agreement with experimental data for applied pump voltages at and below about 5 V. This applied pump voltage is approximately the value required to prevent flooding. The model is therefore a good engineering tool in designing

and estimating pump characteristics for fuel cell water removal and flooding prevention. Our results show some deviations between the theoretical and experimental arise due to increasing acidity in the pump and the drainage of the wick that was integrated with the pump. With constant EO pump operation, we identified that an EO pump voltage of 5 V is the minimum to prevent flooding at a fuel cell current density of $0.5\,A\,cm^{-2}$ with fully humidified gases. In addition, we found that complete water removal is not necessary to prevent flooding; the pump needs only remove about 36% of the product water to prevent flooding. For this case, the parasitic load of the EO pump was negligible at 0.07%.

Acknowledgements

References

[1] Hydrogen, Fuel Cells & Infrastructure Technologies Program: Multi-Year Research Development and Demonstration Plan, U.S. Dept of Energy, 2007.
[2] Y. Sone, P. Ekdunge, D. Simonsson, J. Electrochem. Soc. 143 (1996) 1254.
[3] R. O'Hayre, S.-W. Cha, W. Collela, F.B. Prinz, Fuel Cell Fundamentals, John Wiley & Sons, New York, 2006.
[4] R.K. Ahluwalia, X. Wang, A. Rousseau, R. Kumar, J. Power Sources 130 (2004) 192.
[5] S.H. Ge, X.G. Li, I.M. Hsing, Electrochim. Acta 50 (2005) 1909.
[6] S.H. Ge, X.G. Li, I.M. Hsing, J. Electrochem. Soc. 151 (2004) B523.
[7] J.S. Yi, J.D.L. Yang, C. King, AIChE J. 50 (2004) 2594.
[8] S. Litster, C.R. Buie, T. Fabian, J.K. Eaton, J.G. Santiago, J. Electrochem. Soc. 154 (2007) B1049.
[9] C.R. Buie, J.D. Posner, T. Fabian, S.-W. Cha, D. Kim, F.B. Prinz, J.K. Eaton, J.G. Santiago, J. Power Sources 161 (2006) 191.
[10] D.G. Strickland, S. Litster, J.G. Santiago, J. Power Sources 174 (2007) 272.
[11] S.H. Yao, J.G. Santiago, J. Colloid Interface Sci. 268 (2003) 133.
[12] S.L. Zeng, C.H. Chen, J.C. Mikkelsen, J.G. Santiago, Sens. Actuators B 79 (2001) 107.
[13] R.F. Probstein, Physicochemical Hydrodynamics, 2 ed., John Wiley & Sons, Hoboken, NJ, 2003.
[14] C.L. Rice, R. Whitehead, J. Phys. Chem. 69 (1965) 4017.
[15] D. Kim, J.D. Posner, J.G. Santiago, Sens. Actuators A 141 (2008) 201.
[16] J.O. Bockris, A.K.N. Reddy, M. Gamboa-Aldeco, Modern Electrochemistry 2A: Fundamental of Electrodics, 2nd ed., Springer, New York, 2000.
[17] B. Viswanathan, S. Sivasanker, A.V. Ramaswamy, Catalysis: Principles and Applications, Alpha Science International Ltd., Oxford, 2002.
[18] V.I. Birss, A. Damjanovic, J. Electrochem. Soc. 130 (1983) 1694.
[19] S.H. Yao, D.E. Hertzog, S.L. Zeng, J.C. Mikkelsen, J.G. Santiago, J. Colloid Interface Sci. 268 (2003) 143.
[20] A. Brask, J.P. Kutter, H. Bruus, Lab on a Chip 5 (2005) 730.
[21] S.K. Vajandar, D.Y. Xu, D.A. Markov, J.P. Wikswo, W. Hofmeister, D.Y. Li, Nanotechnology 18 (2007).
[22] R.J. Hunter, Zeta Potential in Colloid Science, Academic Press, London, 1981.
[23] P. Pei, M. Ouyang, Q. Lu, H. Huang, X. Li, Int. J. Hydrogen Energy 29 (2004) 1001.
[24] F. Barbir, PEM Fuel Cells: Theory and Practice, Elsevier Academic Press, London, 2005.
[25] M. Oszcipok, D. Riemann, U. Kronenwett, M. Kreideweis, A. Zedda, J. Power Sources 145 (2005) 407.
[26] R.C. McDonald, C.K. Mittelsteadt, E.L. Thompson, Fuel Cells 4 (2004) 208.